Front Tracking for Gas Dynamics

I-L. CHERN

Institute of Mathematics, Academia Sinica, Nankang, Taipei, Taiwan, Republic of China

AND

J. GLIMM,*,†,‡ O. McBRYAN,*,§ B. PLOHR,* AND S. YANIV,*,†

Courant Institute of Mathematical Sciences, New York University, New York, New York 10012

Front tracking is an adaptive computational method in which a lower dimensional moving grid is fitted to and follows the dynamical evolution of distinguished waves in a fluid flow. The method takes advantage of known analytic solutions, derived from the Rankine–Hugoniot relations, for idealized discontinuities. In this paper the method is applied to the Euler equations describing compressible gas dynamics. The main thrust here is validation of the front tracking method: we present results on a series of test problems for which comparison answers can be obtained by independent methods. © 1986 Academic Press, Inc

1. INTRODUCTION

Front tracking is an adaptive computational method for modeling fluid flow. Its goal, shared with adaptive methods in general, is to obtain increased resolution by using special computational degrees of freedom that (a) are placed (in space and time) where they are most needed, and (b) fit the nature of the solution as closely as possible. Within this general framework, tracking is distinguished by the choice of a lower dimensional adaptive grid, called the front or the interface, as its special computational degree of freedom. Thus for flow problems in two space dimensions, tracking employs a moving one-dimensional grid, i.e. a system of curves, in addition to a two-dimensional grid. Furthermore these curves are not purely geometrical, but are associated with physical waves in the solution. They are defined implicitly by the solution, and they evolve dynamically with it.

The problems for which tracking is an attractive method are those containing

discontinuities and other singularities concentrated on surfaces (curves in two dimensions). Such singularities abound in compressible fluid dynamics: they include shock waves, contact discontinuities, material interfaces, phase boundaries, slip lines, and chemical reaction fronts.

What about the internal structure of the discontinuity? Sharp discontinuities exist as solutions of mathematical equations (e.g., the Euler equations) that describe idealized physics. The missing physics and corrected equations are usually known (e.g., the Navier–Stokes equations), and so are the parameters that govern the correction (e.g., the viscosity). Such a parameter often defines a length scale that measures the width of the discontinuity. For many flow problems this length is much smaller than realistic computational mesh lengths, so that two possibilities arise: either the physics at subgrid levels can be ignored and tracking based on the idealized equations is adequate for modeling the physics; or subgrid physics cannot be ignored and local mesh refinement must be used to resolve the internal structure of the discontinuity. There are problems of both types, and there are problems with multiple length scales that combine these types (so that the discontinuity, once resolved, contains a further sharp discontinuity within it).

Early proposals for tracking are described in Richtmyer and Morton [20]. These ideas were further developed by Moretti [18]. These solutions are of high quality but appear to be limited to somewhat simplified situations. The goal of the work reported here is to implement a general purpose computational package based on front tracking ideas that provides highly resolved solutions for partial differential equations. At present it is applicable to problems with important discontinuities that contain ignorable subgrid physics. The current effort is based on systematic use of data structure and modular programming concepts. Our implementation is designed to allow flexible adaptation to a variety of fluid problems. Parallel efforts using many of the same computational modules have been directed at incompressible two-phase flow in oil reservoirs [10, 7, 8] and instabilities in fluid interfaces [13].

In this paper we describe the algorithm used to solve a hyperbolic system of nonlinear conservation laws

$$\mathbf{w}_t + \nabla \cdot \mathbf{f}(\mathbf{w}) = 0. \tag{1.1}$$

While most of the discussion will be valid for general systems of conservation laws, we will be concerned specifically with the Euler equations for a compressible, inviscid, polytropic gas, for which

$$\mathbf{w} = \begin{pmatrix} \rho \\ \mathbf{m} \\ E \end{pmatrix} \quad \text{and} \quad \mathbf{f}(\mathbf{w}) = \begin{pmatrix} \mathbf{m} \\ \dfrac{\mathbf{m}\mathbf{m}}{\rho} + p \\ \dfrac{\mathbf{m}}{\rho}(E + p) \end{pmatrix}. \tag{1.2}$$

Here ρ is the mass density of the fluid, $\mathbf{m}$ is the momentum density ($\mathbf{m} = \rho\mathbf{v}$, where $\mathbf{v}$ is the fluid velocity), E is the total energy density, and p is the thermodynamic pressure, specified by the polytropic equation of state

$$p = (\gamma - 1)[E - |\mathbf{m}|^2/2\rho] \tag{1.3}$$

for some contant $\gamma > 1$. These equations embody, respectively, the conservation of mass. Newton's law, and the conservation of energy.

We have tested the resolution of the front tracking method, as applied to gas dynamics, by solving model problems on coarse or moderate grids. The results of these tests are desribed in Section 6. In principle, tracking also applies to complicated problems on fine grids if fast computers are used, and it applies to problems (such as combustion) for which subgrid physics is not ignorable if a mesh refinement algorithm is incorporated, but these steps have not yet been taken.

We conclude this introduction with a comparison of our progress on front tracking relative to some of the standard difficulties which have been encoutered in previous efforts to implement this method. Briefly we have solved some but not all of these standard difficulties. Because of the general framework being used, the authors believe that there is a good chance to overcome most of the remaining difficulties. We are grateful to one of the referees for supplying the following list of classic difficulties for front tracking.

1. Achieving second-order accuracy at a shock without post-shock oscillations.

2. Avoiding stringent limits on the time step arising in the bits and pieces of zones which are crossed by a tracked front.

3. Properly treating slip along a front.

4. Treating (a) highly distorted fronts, and (b) changes of the topology of regions bounded by fronts from simply connected to multiply connected regions.

5. Treating collisions and intersections of fronts with other fronts and with boundaries.

6. Treating the disappearance of weakening fronts and the appearance of new fronts at boundaries or at collisions of other fronts.

The status of front tracking on these six difficulties is as follows:

1. This problem is solved on a conceptual level, but needs a second-order-accurate Riemann solver to complete the numerical implementation.

2, 3, and 4a. These problems appear to be fully solved.

4b, 5, and 6. There is work in progress on these problems, about which we make no comment at the present time. A partial solution to these problems for petroleum reservoirs is shown in [9].

Not all scientific and numerical issues associated with the propagation of nodes have been fully resolved, nor have all node types been implemented at the present time. There is work in progress on both of these points.

2. Concepts and Data Structures

In this section we describe the data structures used in our implementation of front tracking. The discussion follows the division of the code into libraries.

2.1. Geometry and Interfaces

The basic data structure defining the geometry and topology of the computational domain is called an interface. An interface in a two-dimensional domain is defined as a collection of oriented curves. A curve starts and ends at nodes, and consists of a doubly linked list of bonds (so that each bond contains a pointer to the next and the previous bond). Associated with each node and with the beginning and end of each bond is a point that defines a position in the plane. In most situations the curves are not allowed to intersect (except at nodes); in this case an interface divides the plane into connected components.

A library of subroutines is devoted to supporting these data structures and performing elementary operations, including creating (i.e., allocating, storing and installing), deleting, copying, printing, and reading these objects. Because linked lists are used, the time needed to add or delete a point is independent of the number of points on the interface. Other routines are available to join or split curves, check for intersections, zoom on subdomains, and compute the topological component containing a given point. This last computation arises frequently and must be efficient. By suitable preprocessing of the interface, this point location problem can be made effectively independent of the length of the interface for non-pathological interfaces [12].

The interface library is described in more detail in a separate publication [12].

2.2. States and Fronts

The interface data structures (and the programing language in which they are written) allow insertion of problem-specific data entries. An interface equipped with data entries specific to front tracking is known as a front. A front contains some general ideas of physics but excludes details of the physical equations being modeled. The principal entries specify the physical nature of curves and nodes and the state variables associated with them.

Curves are of two types: boundary curves and physical curves. A boundary curve is further classified as being a periodic boundary, a Dirichlet boundary (coupling to ambient reservoir), or a Neumann boundary (acting as a reflecting boundary). The various physical types of curves are defined by the physics being modeled. For gas dynamics the physical curves are sound waves (including shocks) and contact discontinuities (including material discontinuities and slip lines). Nodes are of three general types: fixed nodes, boundary nodes, and physical nodes. A fixed node joins boundary curves; for example, it can demarcate a corner in a wall or separate curves corresponding to different boundary conditions. At a boundary node a single physical curve meets a boundary curve, such as when a shock moves normally

along a wall. The classification of physical nodes for gas dynamics is given in Section 5.

Throughout most of the code, a state is the location of a segment of storage with a fixed size. Exactly what information is stored in a state depends on the physics being modeled, but only a few of the lowest-level subroutines (e.g., the Riemann problem solver and the Lax-Wendroff elementary integration step) depend on the specific form of this information. For gas dynamics there are four real numbers, specifying the density, two components of monumentum density, and the energy density, together with the adress of the data base describing the equation of state. Since a curve in the front presents a physical wave across which there is, in general, a discontinuity in the solution, there are two states associated with each point of a curve, corresponding to its two sides. At a node there is a state associated with each component adjacent to it. For convenience, however, we associate these states with the ends of the curves that meet at the node, rather than with the node itself.

The front library is a collection of subroutines that support states, boundary conditions, and the data management and geometrical aspects of the dynamical propagation of curves and nodes. All physics-dependent operations are confined to a few subroutines that are accessed through pointers to functions that are defined in a physics library. Briefly, the dynamical propagation of the front is a follows. For each curve there are two sweeps over its points: the first employs a physics-dependent subroutine that moves each point and updates its associated states in accordance with waves propagating normally to the curve; the second constructs a three-point stencil of states centered at each point and calls a physics-dependent subroutine that updates the center state by taking account of waves moving tangentially to the curve. The points in the vicinity of each node are propagated so as to allow for interaction of the waves meeting at the node. For fixed and boundary nodes this can be accomplished using the subroutine that propagates a point together with geometrical constructions; for physical nodes specialized routines are called. The front is then remeshed according to one of several algorithms designed to redistribute points to enhance curvature resolution and to prevent pile-ups and thinning. To define the states at new front mesh points the remeshing subroutine uses a physics-dependent subroutine to interpolate between nearby states belonging to the same component. Finally the front is checked for self-intersections. If intersections are found, a physics-dependent subroutine that untangles the front is called. Further details on the propagation of the front are given in Section 4.

2.3. *Interior Waves*

The region away from the curves defining the front is called the interior. Since the curves represent possible discontinuities in the solution, each component of the interior is regarded as the domain for a separate initial/boundary-value problem. Depending on the physics being modeled, elliptic, parabolic, or hyperbolic equations are to be solved. For gas dynamics the system is hyperbolic, so we will

restrict our attention here to a library of routines for solving hyperbolic equations, especially hyperbolic conservation laws.

State variables in the interior are associated with points on a rectangular grid. Each grid point belongs to a specific component. The value of the solution at an arbitrary position in the computational domain is obtained through bilinear inter-polation of interior states or, in case the position is close to the front, through linear interpolation between interior states and states on the front belonging to the same component. The calculation of such states is necessary in the normal propagation sweep along the front, so care is taken to divide each component into triangular elements that enable efficient interpolation.

To update the interior states in time a number of schemes are provided. At present the random choice, scalar upwind, and Lax–Wendroff schemes using spatial operator splitting, as well as a fully two-dimensional Lax-Wendroff scheme, have been implemented. It is critical to the front tracking method that the states used in the stencils for these schemes all belong to the same component. In our application to gas dynamics we have used the Lax-Wendroff schemes, which we describe further in Section 3.

2.4. *Utilities and Drivers*

Various general purpose routines for storage allocation, debugging, and input/output are contained in a utility library. Routines that govern the control flow of the time loop, initialization, diagnostic analysis of the solution, and printing are contained in a driver library. Also in the driver library are routines that specially format the input and output to interface to a package of data analysis and graphics programs.

2.5. *Physics Subroutines*

As indicated above, certain operations on state variables and points on the front ultimately depend on the physics being modeled. All of these features have been isolated in a handful of subroutines that are accessed though abstract function pointers. For gas dynamics the key subroutines needed are: the subroutine that propagates a point, which is essentially a non-local Riemann problem solver; the subroutine that updates the states during the tangential sweep of the front, which is a one-dimensional Lax-Wendroff operator; the specialized subroutines that propagate physical nodes, which solve two-dimensional Riemann problems; and the stencil operator for the interior scheme, which is a one- or two-dimensional Lax-Wendroff operator. These subroutines will be described in the following. In addition there is the subroutine that initializes the front and interior according to the test problem being studied along with miscellaneous subroutines for diagnostic analysis and printing of the solution.

3. THE INTERIOR SCHEME

The numerical approximation to the solution of the non-linear conservation law (1.1) is represented by state variables at the nodes of a rectangular grid together with double-valued state variables at the points on an interface. The solution at an arbitrary position in the computational domain is obtained by interpolating among these interior and front states, as we now describe. The interpolation position lies in some rectangular grid block defined by four grid nodes; it is also regarded as lying in some specified topological component. Since the front represents a possible dis-continuity in the solution, it is important not to interpolate between states corresponding to different components. If the four grid nodes all lie in the same component as specified, then we may obtain the solution using bilinear interpolation. If, however, not all of the grid nodes lie in the same component, the front cuts through the grid block to separate the grid nodes from one another. In this case only the grid nodes that lie in the specified component of the interpolation position, together with states on the appropriate side of the front, are used in the interpolation. Thus we triangulate each grid block that is crossed by the interface and use linear interpolation on these triangular elements. Our present triangulation scheme determines the points on the front where it crosses the vertical and horizontal grid lines; these points, along with the grid nodes lying in the correct component, define the corners of the triangles. In this scheme it is computationally efficient to determine the triangle in which the interpolation point lies, since in all but one case the triangles are arranged in a star-like fashion about one common corner.

For the calculation of the solution in the interior regions we use either an operator split one-dimensional Lax–Wendroff or a fully two-dimensional Lax–Wendroff scheme. Here we discuss only the two-dimensional (unsplit) scheme. The two-dimensional scheme involves two half steps. To facilitate the coupling of the front and the interior, the front is also advanced in half steps. Since the Lax–Wendroff scheme is a leapfrog composition of two Lax–Friedrichs steps it is enough to describe the Lax–Friedrichs scheme. This scheme usually assumes the initial data to be known at the four corners of a square. In our application, however, there are irregular squares, i.e., squares for which one or more of their corners are cut off by the front and thus lies in the wrong component. To circumvent this difficulty we view the Lax–Friedrichs scheme as defined by a flux balance: the sum of the fluxes through the sides of a mesh block determines the change in time of a conserved quantity integrated over the block. From this point of view the Lax–Friedrichs scheme is defined for irregular squares as well as regular squares. In fact, the propagation of the front also determines the fluxes through the front and thereby through the sides of the irregular squares. The triangulation that is constructed for interpolating the solution is used to define these irregular squares.

To be more explicit, consider a particular grid block with side length Δx. Given the solution at time t_0, we wish to calculate the solution at the center x_c of this block at time $t_1 = t_0 + \Delta t/2$. The center of the grid block lies in some topological

component at the later time t_1, and it is the solution in this component that we wish to evaluate. Let $A(t)$ denote the portion at time t of the grid square lying in this component, and let $|A(t)|$ denote its area. Then by integrating the conservation law (1.1) over this region and then integrating in time from t_0 to t_1 we obtain

$$\int_{A(t_1)} \mathbf{w}(\mathbf{x}, t_1)$$

$$= \int_{A(t_0)} \mathbf{w}(\mathbf{x}, t_0) + \int_{t_0}^{t_1} dt \int_{\partial A(t)} \sigma(\mathbf{x}, t)\, \mathbf{w}(\mathbf{x}, t) - \int_{t_0}^{t_1} dt \int_{\partial A(t)} \hat{\mathbf{n}}(\mathbf{x}, t) \cdot \mathbf{f}(\mathbf{w}(\mathbf{x}, t)). \quad (3.1)$$

Here $\hat{\mathbf{n}}(\mathbf{x}, t)$ and $\sigma(\mathbf{x}, t)$, for points $\mathbf{x}$ on the boundary $\partial A(t)$, are the unit normal vector and the normal speed of the boundary. Thus for points $\mathbf{x}$ on the tracked front, $\sigma(\mathbf{x}, t)$ is the normal speed of the front, while for other points it vanishes. In order to obtain a numerical approximation to this formula that is stable, we note the identity

$$\int_{t_0}^{t_1} dt \int_{\partial A(t)} \sigma(\mathbf{x}, t)\, \bar{\mathbf{w}} = (|A(t_1)| - |A(t_0)|)\, \bar{\mathbf{w}} \qquad (3.2)$$

for any constant state $\bar{\mathbf{w}}$. By suitably choosing $\bar{\mathbf{w}}$ we can arrange that the integral on the left in (3.2) approximates the second integral on the right in (3.1) with relative error $O(\Delta x^2)$. For instance, if the front at time t_0 consists of a single line segment crossing the grid block, then we can take $\bar{\mathbf{w}}$ to be the solution on the front at the center of this segment. By approximating the other integrals in (3.1) we obtain the formula

$$|A(t_1)|\, \mathbf{w}(\mathbf{x}_c, t_1) = |A(t_0)|\, \mathbf{w}_0 + (|A(t_1)| - |A(t_0)|)\, \bar{\mathbf{w}}$$

$$- \frac{\Delta t}{2} \int_{\partial A(t_0)} \hat{\mathbf{n}}(\mathbf{x}, t_0) \cdot \mathbf{f}(\mathbf{w}(\mathbf{x}, t_0)) + O(\Delta t^2 \, \Delta x^2) + O(\Delta t \, \Delta x^3), \quad (3.3)$$

in which $\mathbf{w}_0$ represents the average value of the solution over the region $A(t_0)$, so that it corresponds to the correct component. If $|A(t_1)|/\Delta x^2$ is not too small, Eq. (3.3) provides a suitable approximation for $\mathbf{w}(\mathbf{x}_c, t_1)$; otherwise $\mathbf{x}_c$ is in general so close to the front that it is appropriate to approximate $\mathbf{w}(\mathbf{x}_c, t_1)$ with states on the front. We note that when the front does not cross the grid square, Eq. (3.3) reduces to the usual Lax–Friedrichs approximation. Finally, the solution at time $t_0 + \Delta t$ is obtained using two Lax–Friedrichs steps in a leapfrog combination.

4. The Front Scheme

The propagation of the front involves the motion of points on the front and the evolution of the states on the front. The propagation of points in the vicinity of

nodes, where in general curves meet, is described in Section 5; here we consider points in the interior of a curve.

Let z_0 be an interior point on the front at time t_0. Points $z^{(0)} = z^{(0)}(s)$ near z_0 are labeled by their arclength displacement s away from $z_0 = z^{(0)}(0)$. A coordinate system for a neighborhood of z_0 is constructed as follows (see Fig. 1). Each pair (r, s) corresponds to the point $x(r, s)$ that is a distance r along the line drawn normal to the front through the point $z^{(0)}(s)$. The coordinate curves $s = \text{const}$ are thus lines perpendicular to the front. Let $\hat{n}(r, s)$ and $\hat{s}(r, s)$ be the parallel translates to $x(r, s)$ of the unit vectors normal and tangent to the front at $z^{(0)}(s)$, respectively. The system

$$w_t + \nabla \cdot f(w) = 0 \tag{4.1}$$

of conservation laws may be written in terms of the normal and tangential derivatives $\hat{n} \cdot \nabla$ and $\hat{s} \cdot \nabla$ as

$$w_t + \hat{n} \cdot [(\hat{n} \cdot \nabla) f(w)] + \hat{s} \cdot [(\hat{s} \cdot \nabla) f(w)] = 0. \tag{4.2}$$

We wish to solve this system subject to the initial conditions $w(t = t_0) = w^{(0)}$, where $w^{(0)}$ is smooth except for possible jump discontinuities across $z^{(0)}$. Let $w^{(e)}$ denote the exact solution at time $t_0 + \Delta t$ to this problem; $w^{(e)}$ is smooth except for possible jumps at the exact front position $z^{(e)} = z^{(e)}(s)$. We say that a computed solution $w^{(c)}$ is correct at the approximate front $z^{(c)} = z^{(c)}(s)$ through order Δt if

$$z^{(e)}(s) = z^{(c)}(s) + O(\Delta t^2) \tag{4.3}$$

and

$$w^{(e)}(z^{(e)}(s), t_0 + \Delta t) = w^{(c)}(z^{(c)}(s), t_0 + \Delta t) + O(\Delta t^2), \tag{4.4}$$

where by this last equation we mean equality of the states on corresponding sides of the jump discontinuities.
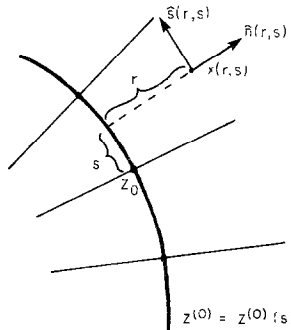

FIG. 1. The local coordinate system used for propagating the front.

The computed solution of system (4.1) is obtained using operator splitting of the system (4.2) in the normal and tangential directions. First the normal equations

$$\mathbf{w}_t + \hat{\mathbf{n}} \cdot [(\hat{\mathbf{n}} \cdot \nabla) \mathbf{f}(\mathbf{w})] = 0, \qquad \mathbf{w}(t = t_0) = \mathbf{w}^{(0)} \tag{4.5}$$

are solved approximately to obtain the computed front position $\mathbf{z}^{(c)} = \mathbf{z}^{(c)}(s)$ and the computed normal solution $\mathbf{w}^{(cn)}$ at time $t_0 + \Delta t$. Then the tangential equations

$$\mathbf{w}_t + \hat{\mathbf{s}} \cdot [(\hat{\mathbf{s}} \cdot \nabla) \mathbf{f}(\mathbf{w})] = 0, \qquad \mathbf{w}(t = t_0) = \mathbf{w}^{(cn)} \tag{4.6}$$

are solved approximately to obtain the solution $\mathbf{w}^{(c)}$ at time $t_0 + \Delta t$.

Let us analyze the error involved in this procedure. The normal front speed $\sigma(s)$ at time t_0 satisfies

$$\mathbf{z}^{(e)}(s) = \mathbf{z}^{(0)}(s) + \Delta t \sigma(s) \, \hat{\mathbf{n}}(0, s) + O(\Delta t^2). \tag{4.7}$$

By Eq. (4.2) and Taylor's theorem,

$$\begin{aligned}
\mathbf{w}^{(e)} (\mathbf{z}^{(e)}(s), t_0 + \Delta t) = \; & \mathbf{w}^{(0)} (\mathbf{z}^{(0)}(s), t_0) + \Delta t \sigma(s) [(\hat{\mathbf{n}} \cdot \nabla) \mathbf{w}^{(0)}](\mathbf{z}^{(0)}(s), t_0) \\
& - \Delta t \hat{\mathbf{n}} \cdot [(\hat{\mathbf{n}} \cdot \nabla) \mathbf{f}(\mathbf{w}^{(0)})](\mathbf{z}^{(0)}(s), t_0) \\
& - \Delta t \hat{\mathbf{s}} \cdot [(\hat{\mathbf{s}} \cdot \nabla) \mathbf{f}(\mathbf{w}^{(0)})](\mathbf{z}^{(0)}(s), t_0) + O(\Delta t^2).
\end{aligned} \tag{4.8}$$

Assume that the computed normal solution $\mathbf{w}^{(cn)}$ is a correct solution at the approximate front $\mathbf{z}^{(c)} = \mathbf{z}^{(c)}(s)$ to the normal equations (4.5) through order Δt. Since the front position obtained by solving the normal equations will agree through order Δt with the exact front position, we conclude that

$$\begin{aligned}
\mathbf{w}^{(cn)}(\mathbf{z}^{(c)}(s), t_0 + \Delta t) = \; & \mathbf{w}^{(0)}(\mathbf{z}^{(0)}(s), t_0) + \Delta t \sigma(s) [(\hat{\mathbf{n}} \cdot \nabla) \mathbf{w}^{(0)}](\mathbf{z}^{(0)}(s), t_0) \\
& - \Delta t \hat{\mathbf{n}} \cdot [(\hat{\mathbf{n}} \cdot \nabla) \mathbf{f}(\mathbf{w}^{(0)})](\mathbf{z}^{(0)})](\mathbf{z}^{(0)}(s), t_0) + O(\Delta t^2).
\end{aligned} \tag{4.9}$$

Assume in addition that $\mathbf{w}^{(c)}$ is a correct solution at the approximate front $\mathbf{z}^{(c)} = \mathbf{z}^{(c)}(s)$ to the tangential equations (4.6) through order Δt. Therefore

$$\begin{aligned}
\mathbf{w}^{(c)}(\mathbf{z}^{(c)}(s), t_0 + \Delta t) = \; & \mathbf{w}^{(cn)}(\mathbf{z}^{(c)}(s), t_0 + \Delta t) \\
& - \Delta t \hat{\mathbf{s}} \cdot [(\hat{\mathbf{s}}(s) \cdot \nabla) \mathbf{f}(\mathbf{w}^{(c)})](\mathbf{z}^{(c)}(s), t_0 + \Delta t) + O(\Delta t^2).
\end{aligned} \tag{4.10}$$

Combining these last two equations shows then that $\mathbf{w}^{(c)}$ is a correct solution at the approximate front $\mathbf{z}^{(c)} = \mathbf{z}^{(c)}(s)$ to the full equations (4.2) through order Δt. In the following we demonstrate how normal and tangential solutions satisfying the above assumptions can be obtained.

First we propagate the front and the states along the front in the normal direction. The solution at time t_0 is evaluated on both sides of the front at $\mathbf{z}_0$, yielding a left and a right state. The solution at time t_0 is also evaluated at a normal distance Δ_r on each side of the front. These states will be used to calculate the waves that

impinge on the front from the interior. Notice that if the front contains curves too close to each other, these new evaluation points $z_0 \pm \Delta r \cdot \hat{n}$ may be in components different from the points $z_0 \pm 0 \cdot \hat{n}$ at the front. In this case the evaluation point is shifted into the correct component. (Conceptually, the state at a point outside a given component is obtained by extrapolation.) Thus we always have as data two left states corresponding to one component and two right states corresponding to a second component.

These states are used as initial data for an extended or non-local Riemann problem. Higher-order solutions of these Riemann problems have been discussed before. To reduce sampling error in the random choice method, a steady-state *Ansatz* has been used [6, 11] to extend local Riemann data over a mesh block, thereby obtaining a non-local Riemann problem, which is solved to higher order. Higher-order Godunov schemes [1, 2] also employ ideas related to solutions of non-local Riemann problems. In the present scheme we solve the non-local Riemann problem as follows.

Using the left and right states located at the front we solve an ordinary Riemann problem. The solution is the correct answer to the non-local problem at time $t_0 + 0$, and it is used to approximate the propagation speeds of the characteristics backward from $t_0 + \Delta t$ to t_0. We find starting points for these characteristics in the normal intervals

$$[z_0 \pm 0 \cdot \hat{n}, z_0 \pm \Delta r \cdot \hat{n}]. \tag{4.11}$$

The states at these points are calculated using linear interpolation between the states on the front and the states at the normally displaced points. In this way we determine which waves from the normal intervals enter the front. Using differential equations in characteristic form together with the Rankine–Hugoniot jump conditions we compute the states to be associated with the propagated front at time $t_0 + \Delta t$.

The solution of the normal sweep along the front is taken as initial values for the tangential sweep. By linear interpolation, the states on each side of the front can be defined everywhere along the front. Therefore we can evaluate the normally propagated solution at each mesh point and at two neighboring points displaced a distance Δs along the front. Using these three stencil points and the one-dimensional Lax–Wendroff scheme, adapted for the tangential equations (4.6), we determine the tangentially propagated state variables. Notice that tangential propagation of the points on the front is equivalent to a remeshing of the front, in the limit $\Delta t \to 0$, so it is not essential to move these points during the tangential sweep.

In what follows the normal sweep is described in more detail for gas dynamics.

4.1. *The Normal Sweep for Shock Waves*

There are two types of shocks for the gas dynamic equations: backward and forward (or 1 and 3) shocks. Here a k-shock is a discontinuity satisfying

$$\lambda_{k-1}(w_l) < \sigma < \lambda_k(w_l) \qquad \text{and} \qquad \lambda_k(w_r) < \sigma < \lambda_{k+1}(w_r), \tag{4.12}$$

where σ is the normal propagation speed of the shock, and $\lambda_1 = u - c$, $\lambda_2 = u$, and $\lambda_3 = u + c$ are the eigenspeeds of normal equations (4.5), $u = \hat{\mathbf{n}} \cdot \mathbf{m}/\rho$ being the normal velocity and $c = (\gamma p/\rho)^{1/2}$ being the speed of sound [21]. Thus there are three characteristics entering each point on the left (right) side and one characteristic entering each point on the right (left) side of a backward (forward) shock. We therefore solve three characteristic equations to obtain the state ahead of the shock, and then solve one characteristic equation together with the Rankine-Hugoniot conditions to obtain the state behind the shock. We shall describe the algorithm for a forward shock only.

The normal equations (4.5) for gas dynamics, as written in characteristic form, are

$$\frac{d}{d\lambda_1}\left(\frac{2c}{\gamma-1} - u\right) = \frac{c}{\gamma}\frac{d}{d\lambda_1} S,$$

$$\frac{d}{d\lambda_2} S = 0, \qquad \frac{d}{d\lambda_2} v = 0, \qquad (4.13)$$

and

$$\frac{d}{d\lambda_3}\left(\frac{2c}{\gamma-1} + u\right) = \frac{c}{\gamma}\frac{d}{d\lambda_3} S,$$

where $v = \hat{\mathbf{s}} \cdot \mathbf{m}/\rho$ is the tangential velocity and $S = \log(p/\rho^\gamma)/(\gamma - 1)$ is the entropy. There are no waves transmitted to the right side of a forward shock, so the characteristic equations determine the state on the right side. We obtain an approximate solution of the characteristic equations by solving the difference equations

$$\frac{2c_r}{\gamma-1} - u_r - \frac{2c_1}{\gamma-1} + u_1 = \frac{(c_r + c_1)}{2\gamma}(S_r - S_1),$$

$$S_r = S_2, \qquad v_r = v_2, \qquad (4.14)$$

and

$$\frac{2c_r}{\gamma-1} + u_r - \frac{2c_3}{\gamma-1} - u_3 = \frac{(c_r + c_3)}{2\gamma}(S_r - S_3),$$

where the subscript r refers to values at time $t_0 + \Delta t$ on the right side of the shock, and the subscripts 1, 2, and 3 refer to values at the feet of the λ_1, λ_2, and λ_3 characteristics at time t_0 (see Fig. 2).

To obtain these states at the feet of the characteristics we first solve the Riemann problem between the left and right states on the front at time t_0 to obtain a preliminary shock position at time $t_0 + \Delta t$. Then the three characteristics, approximated as straight lines, are drawn backward from the shock position at
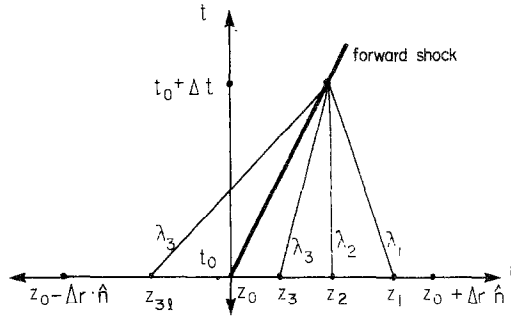
FIG. 2. The characteristic curves for a forward shock.

$t_0 + \Delta t$ to foot positions in the normal interval $[z_0, z_0 + \Delta r \cdot \hat{\mathbf{n}}]$ at time t_0. The corresponding states are obtained using linear interpolation between the right state at $\mathbf{z}_0$ and the state at $\mathbf{z}_0 + \Delta r \cdot \hat{\mathbf{n}}$. Using these states in the above difference approximation to the characteristic equations yields a right state at time $t_0 + \Delta t$ that is correct through order Δt.

On the left side of the shock only the λ_3 characteristic impinges on the shock. The corresponding characteristic equation is approximated by the difference equation

$$\frac{2c_l}{\gamma - 1} + u_l - \frac{2c_{3l}}{\gamma - 1} - u_{3l} = \frac{(c_l + c_{3l})}{2\gamma}(S_l - S_{3l}), \qquad (4.15)$$

where the subscript $3l$ refers to values at the foot of the left λ_3 characteristic. The Rankine–Hugoniot conditions for a forward shock are

$$v_l = v_r, \qquad \frac{\rho_l}{\rho_r} = \left(\frac{\gamma + 1}{\gamma - 1}\frac{p_l}{p_r} + 1\right)\Big/\left(\frac{\gamma + 1}{\gamma - 1} + \frac{p_l}{p_r}\right),$$

and

$$u_l - u_r = \frac{1}{\gamma}c_r \cdot \left(\frac{p_l}{p_r} - 1\right)\Big/\left[1 + \frac{\gamma + 1}{2\gamma}\left(\frac{p_l}{p_r} - 1\right)\right]^{1/2}. \qquad (4.16)$$

Given the solution obtained above for the state $\mathbf{w}_r$ on the right side of the shock, the characteristic and Rankine–Hugoniot equations yield an approximate left state at time $t_0 + \Delta t$ that is correct through order Δt. Finally, the propagation speed of the shock is calculated by averaging the shock speeds at time t_0 and at time $t_0 + \Delta t$.

4.2. The Normal Sweep for Contact Discontinuities

A contact discontinuity separates two states having different values of density and tangential velocity but the same values of pressure and normal velocity. The

propagation speed of a contact is the normal particle speed u, so only one family of characteristics on each side enters the discontinuity. Thus we have

$$\frac{d}{d\lambda_1}\left(\frac{2c}{\gamma-1}-u\right)=\frac{c}{\gamma}\frac{d}{d\lambda_1}S \quad \text{and} \quad \frac{d}{d\lambda_3}\left(\frac{2c}{\gamma-1}+u\right)=\frac{c}{\gamma}\frac{d}{d\lambda_3}S \quad (4.17)$$

on the right and left sides of the contact, respectively. In addition the entropy and the tangential velocity on each side of the contact is constant.

The corresponding difference equations are

$$\frac{2c_r}{\gamma-1}-u_r-\frac{2c_{1r}}{\gamma-1}+u_{1r}=\frac{c_r+c_{1r}}{2\gamma}(S_r-S_{1r}),$$

$$S_r=S_{2r}, \qquad S_l=S_{2l}, \qquad v_r=v_{2r}, \qquad v_l=v_{2l}, \qquad (4.18)$$

and

$$\frac{2c_l}{\gamma-1}+u_l-\frac{2c_{3l}}{\gamma-1}-u_3=\frac{c_l+c_{3l}}{2\gamma}(S_l-S_{3l}),$$

where the subscripts l and r refer to left and right values, respectively, at time $t_0+\Delta t$, while the subscripts $1r$ and $2r$ refer to values at the feet of the right λ_1 and λ_2 characteristics at time t_0, and the subscripts 2_l and 3_l refer to values at the feet of the left λ_2 and λ_3 characteristics at time t_0 (see Fig. 3). These states at the feet of the characteristics are obtained by linear interpolation in the same fashion as described for shock waves. In addition to the characteristic equations we have the Rankine–Hugoniot conditions that $u_l=u_r$ and $p_l=p_r$ for a contact. By solving these equations we obtain an approximate solution to the normal equations that is correct at the front through order Δt. The propagation speed of the contact is calculated, as for shocks, by averaging the speeds at time t_0 and at times $t_0+\Delta t$.
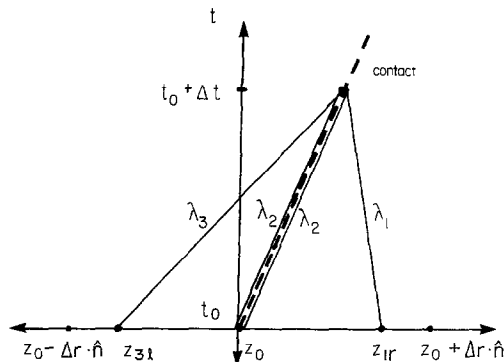

FIG. 3. The characteristic curves for a contact discontinuity.

4.3. *The Normal Sweep for Boundaries*

The boundaries are considered as part of the front, and the states on the boundaries are updated using the normal/tangential operator splitting method. The boundary conditions under consideration are either Dirichlet or Neumann. Periodic boundary conditions are implemented so as to have no effect on the solution and are not discussed further.

Dirichlet boundary conditions for the gas dynamics equations are defined physically as the coupling to an ambient reservoir (inlet or outlet). Mathematically, they are defined by the specification of a boundary state. This state plays the role of far-field conditions. Information about the far-field conditions are propagated into the computational region only by incoming characteristics.

Let $\mathbf{w}_l$ and $\mathbf{w}_r$ be the left and right states at a given point $\mathbf{z}_0$ on the boundary. Let $\mathbf{w}_{ll}$ be the state at a normal distance Δr on the left side, and $\mathbf{w}_{rr}$ the state at a normal distance Δr on the right side of the boundary. If the exterior of the computational region is on the left (right), $\mathbf{w}_{ll}$ ($\mathbf{w}_{rr}$) is the far-field boundary condition. To obtain the normally propagated solution at the boundary we first perform a Lax–Wendroff step using $\mathbf{w}_{ll}$, $\mathbf{w}_l$, and $\mathbf{w}_r$ as the values at the points $\mathbf{z}_0 - \Delta r \cdot \hat{\mathbf{n}}$, $\mathbf{z}_0$, and $\mathbf{z}_0 + \Delta r \cdot \hat{\mathbf{n}}$, respectively, obtaining the intermediate state $\mathbf{w}_l^{(i)}$. We do the same on the right side of the curve obtaining $\mathbf{w}_r^{(i)}$. Then the computed normal left and right states $\mathbf{w}_l^{(c)}$ and $\mathbf{w}_r^{(c)}$ are obtained by solving the Riemann problem between the intermediate states $\mathbf{w}_l^{(i)}$ and $\mathbf{w}_r^{(i)}$.

At Neumann boundary curves we require that the normal velocity vanish. Thus only one sonic characteristic, λ_1 or λ_3, impinges on the wall. Suppose the computational region is on the right side of the boundary. Just as in the case of a contact discontinuity, but taking into account that the normal velocity u vanishes at the boundary, the characteristic equations may be approximated by the different equations

$$S = S_2, \qquad v = v_2,$$

and

$$\frac{2c}{\gamma - 1} - \frac{2c_1}{\gamma - 1} + u_1 = \frac{c + c_1}{2\gamma}(S - S_1), \tag{4.19}$$

where the subscripts 1 and 2 refer to values at the feet of the λ_1 and λ_2 characteristics at time t_0. These equations may be solved to yield a solution to the normal equations that is correct through order Δt.

5. TWO-DIMENSIONAL RIEMANN PROBLEMS

An intersection of two or more curves of an interface is called a node. In the context of front tracking, a node is the center of the interaction of the waves meeting at

a point. In contrast to the problems discussed in Section 4, the geometry near a node does not necessarily admit resolution into normal and tangential components, so its evolution cannot be determined by solving a sequence of one-dimensional problems.

A node is categorized by the (circular) ordering and the types of the waves emanating from it. In the near vicinity of a node the curves are approximately straight lines that separate wedge-shaped regions. Thus we are led to define a two-dimensional Riemann problem to be an initial value problem for a two-dimensional conservation law having data that is either piecewise constant or is a simple centered rarefaction wave in each of a finite number of wedges. The form of the data is thus

$$\mathbf{w} = \mathbf{w}_j \qquad \text{for} \quad \theta_{j-1} < \theta < \theta_j \tag{5.1}$$

for $j = 1, ..., n$, where $\theta_0 = \theta_n$, and each $\mathbf{w}_j$ is either a constant or a centered wave. Such problems have been studied for scalar conservation laws [14, 16, 23], but only special solutions are known for systems of conservation laws. In analogy with the solution of one-dimensional Riemann problems, the solution of a two-dimensional Riemann problem will evolve into a more complicated configuration containing several nodes (two-dimensional elementary waves interactions) moving apart from one another.

We simplify the problem in two ways. First we look for elementary wave interactions. These are recognized as being stable under forward time evolution and are associated with a single node in the solution of a general Riemann problem. Second we restrict ourselves to problems that are generic under change of initial conditions, and to solutions that are limits of viscous solutions as the viscosity parameter tends to zero. At this point physical intuition and a knowledge of experimental facts allow a guess concerning a (nearly complete?) list of elementary wave interactions. Even under further restrictions (such as a polytropic gas with only small amplitude waves) there seems to be no mathematical analysis of the problem of classifying elementary waves in two-dimensional Riemann problems (see [24]).

As mentioned in Section 2.2, a node is either a fixed node, a boundary node, or a physical node. At a fixed node only boundary curves meet. Here we describe the case when only two boundary curves meet. Such a node is, for example, a corner of a wall (when both curves are of Neumann type) or the end of an inlet or outlet (where there is a transition from Neumann to Dirichlet boundary conditions). Its propagation involves only the dynamics of the state variables associated with the node. In the case of orthogonal curves the updated states are determined using operator splitting in the directions normal and tangential to one of the curves. For transitions from Neumann to Dirichlet boundaries meeting at general angles this algorithm should also be correct. In the case of an arbitrary angle between walls we use a scheme in which flux through a polygonal element near the corner is balanced to obtain the states around the node.

The general phenomena at a node where a physical curve interacts with a boundary curve appear to be as follows. If the boundary curve is of Dirichlet or periodic

type, no interaction between the boundary and the physical wave occurs. Thus normal/tangential splitting is correct so long as the states at positions outside of the computational region are obtained by applying the appropriate boundary condition. We therefore restrict the discussion to the interaction of a physical wave with a Neumann boundary, i.e., a wall. For a general conservation law, any physical wave can meet a flat wall normally; again normal/tangential splitting is correct. For gas dynamics a single wave meeting a wall obliquely can only be a contact discontinuity: a slip line can meet a wall only tangentially, and a shock wave can only meet a wall normally, since the normal velocity at the wall must be zero. Configurations in which two or more waves meet at the wall can occur, however. In the regular reflection of a shock wave, two shock waves meet at a wall, one being incident (incoming to the wall), the other being reflected. A shock can also meet a smooth portion of a wall obliquely in the presence of a slip line. In effect the slip is equivalent to a corner in the wall and the oblique shock is an attached bow shock. Such flow can occur in supersonic nozzle flow and leads to boundary separation. Additional phenomena, for instance the attached bow shock, occur in the presence of discontinuities in the boundary, such as at a corner of a wall or at an inlet. In the case of one physical wave the propagation of the node is obtained by operator splitting in the normal and tangential directions to the physical curve. In the case of two waves, one incident and the other reflected, we use the Rankine–Hugoniot conditions for the incident wave and shock polar calculations [3] to obtain the angle of reflection and the states around the node. As with the one-dimensional Riemann problem, non-local information should be (and, in most cases implemented, is) used to compute the effects of waves entering or transmitted through the node.

The same ideas apply to the classification of interior nodes. In fact a contact discontinuity serves as a reflection surface for shock waves, so that one or two shock waves may appear on each side of the contact. The sound speeds on either side of the contact generally differ. Moreover the speed of an incident shock as it moves along a contact depends on the angle it makes with the contact. Using both sound speeds and incident angles, a fast side and a slow side of the contact can be identified. On the fast side the wave configuration is either a normal shock or a regular reflection, while on the slow side a single transmitted shock occurs. Because the contact can bend at the point of incidence of the shock, the reflected wave can be a

transmitted shock, a contact, and a reflected rarefaction wave. The Mach stem configuration is yet another node type. A three-wave interaction is the generic configuration for contact waves. The classification becomes more complicated when waves ending at points of zero strength are allowed. The propagation of these interior nodes is not implemented at present.

6. VALIDATION

We present four series of calculations that test the two-dimensional propagation of discontinuous waves. The modes of wave propagation in two dimensional gas dynamics are shock waves (nonlinear sound waves), contact discontinuities (temperature fronts), and slip lines (transverse velocity discontinuities). The problems testing these modes are chosen to allow verification by means of independent solutions.

6.1. *Circularly Symmetric Problems*

In our first series of tests we study the propagation of curved shock waves and contact discontinuities evolving from circularly symmetric initial data. An initial pressure discontinuity across a circle gives rise to two discontinuous waves, a shock and a contact. For these problems the comparison solution is obtained by an elementary one-dimensional calculation exploiting the radial symmetry. This calculation uses the random choice method, together with a time-splitting step that takes account of the source term introduced by the change in coordinates [22]. In the front tracking method it is necessary to track the contact wave as well as the shock, since otherwise the Lax–Wendroff interior scheme is too unstable on reasonable grids.

In Figs. 4a–d are shown the results of a calculation on a 40×40 grid in which the pressure inside the initial circle is 100 times higher than outside. Figure 4a shows the positions of the contact (the inside circle) and the shock (the outside circle) together with the velocity vectors at a time midway in the run. The corresponding density and pressure profiles as a function of radius are shown in Figs. 4b and c. In these profiles the solid curve is the result from the one-dimensional calculation, while the vertical error bars extend from the minimum to the maximum values in the two-dimensional solution at fixed radii, indicating the angular dependence of the solution. In Fig. 4d the contact and shock positions are plotted vs time, with the solid curve showing the comparison answer, and the dots showing the radii of the two-dimensional fronts. The deviation of these fronts from circles is too small to be plotted in this figure.

Similarly, Figs. 5a–d show the results for a calculation in which the pressure on the inside is 100 times smaller than on the outside. Since for this run there is an outward moving rarefaction, a circular reflecting wall (the outermost circle in Fig. 5a) was introduced in order to preserve the circular symmetry of the problem.

6.2. *Supersonic Flow past a Wedge*

The supersonic flow past a wedge in a channel was tested by comparing the solution with the solution of the steady-state solution obtained by the method of characteristics [17]. In this test a bow shock generated by a Mach 3 flow over a 30° wedge interacts with a Prandl–Meyer expansion. The initial data for the two-dimensional calculation was a slight perturbation of the steady-state solution
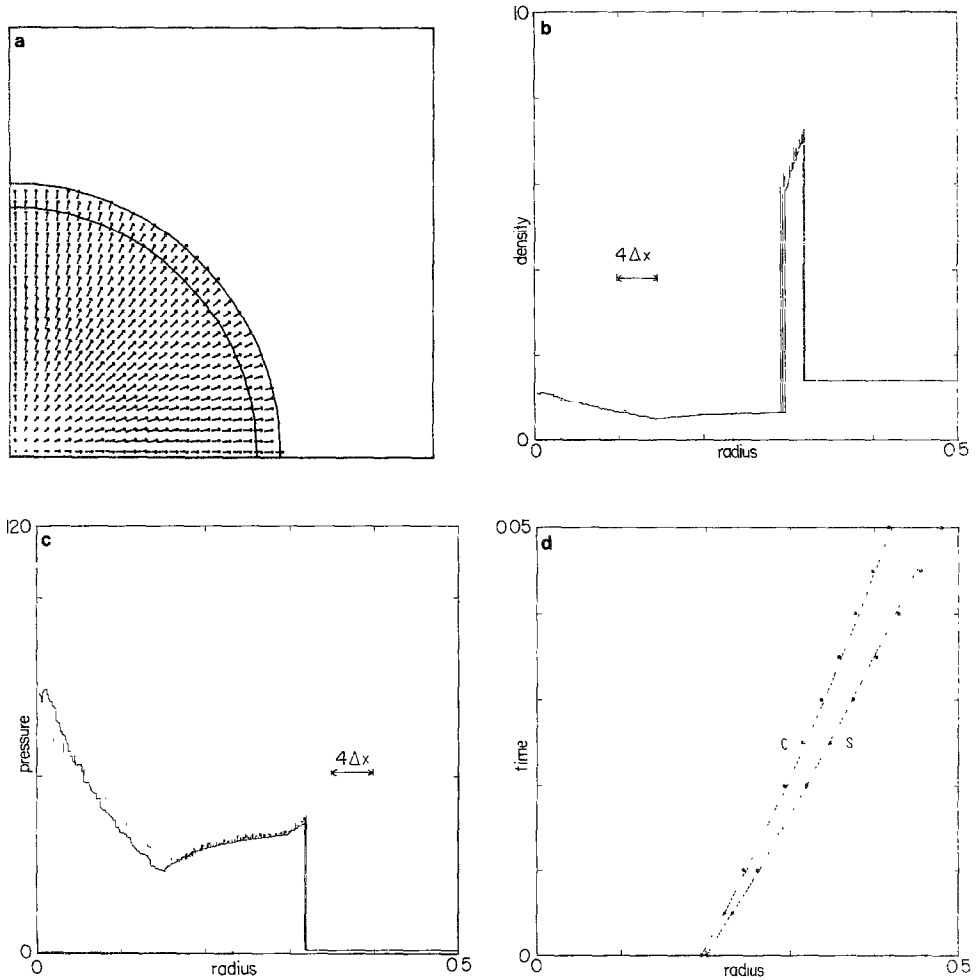
FIG. 4. (a) The shock wave (outer circle), the contact discontinuity (inner circle), and the velocity vectors are pictured for a circularly symmetric computation using a 40 × 40 grid. The initial conditions consisted of uniform density, zero velocity, and a circular pressure discontinuity at radius 0.2 with pressure ratio, inside to outside, of 100. The time it takes a sound wave in the region inside of the contact to travel 0.4 times the width of the computational region has elapsed. (b). A plot of density vs radius corresponding to (a) is shown. The solid curve shows the results obtained in a one-dimensional calculation using the random choice method. The vertical lines represent the range of density values in the two-dimensional solution at a fixed radius as the angle varies. Thus the vertical lines show the angular dependence in the solution. (c). A plot of pressure vs radius corresponding to (a) is shown. The solid curve and the vertical lines represent the one- and two-dimensional results, as explained in the caption to (b). (d). A plot of the radius of the contact discontinuity (C) and the radius of the shock wave (S) as functions of time is presented. The solid curves were obtained by passive tracking in the one-dimensional random choice solution. The dots represent radius values in the two-dimensional solution. The angular dependence of the radius, i.e., the deviation of the tracked front from a circle, is too small to plot.
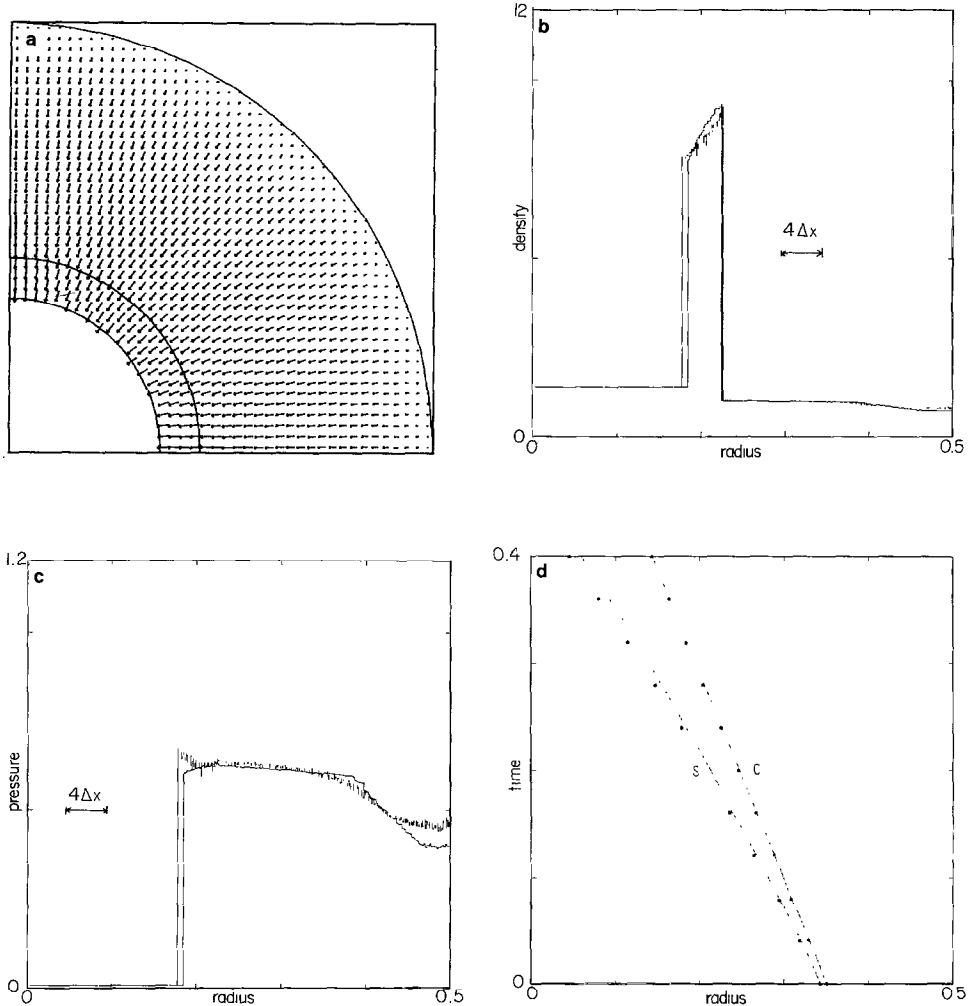
FIG. 5. (a) The shock wave (inner circle), the contact discontinuity (outer circle), and the velocity vectors are pictured for a circularly symmetric computation using a 40×40 grid. The initial conditions consisted of uniform density, zero velocity, and a circular pressure discontinuity at radius 0.35 with pressure ratio, inside to outside, of 0.01. The time it takes a sound wave in the region outside of the contact to travel 0.48 times the width of the computational region has elapsed. The outermost circle is a reflecting wall, introduced to maintain circular symmetry. (b). A plot of density vs radius corresponding to (a) is shown. The solid curves and the vertical lines represent the one- and two-dimensional results, as explained in the caption to Fig. 4b. (c). A plot of pressure vs radius corresponding to (a) is shown. The solid curves and the vertical lines represent the one- and two-dimensional results, as explained in the caption to Fig. 4b. (d). A plot of the radius of the contact discontinuity (C) and the radius of the shock wave (S) as functions of time is presented. The solid curves and the dots represent the one- and two-dimensional solutions, as explained in the caption in Fig. 4d.
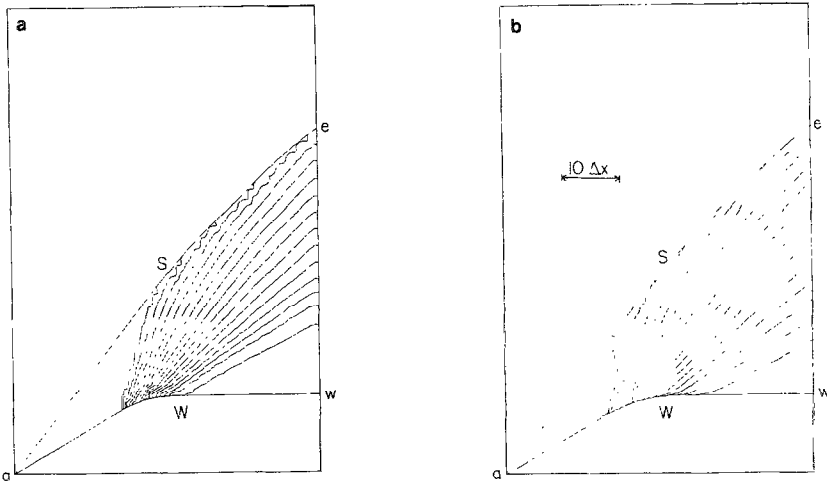
FIG. 6. (a) The position of the bow shock (S) and the isopycnic (constant density) contours are shown for the steady-state flow configuration obtained when parallel supersonic flow with Mach number 3 impinges from the left on a 30° wedge (W). These data were calculated using a one-dimensional random choice method for steady, supersonic flow. (b) The position of the bow shock (S) and the isopycnic contours, as obtained in a time-dependent calculation on a 50×50 grid starting from the steady-state flow conditions of (a), are shown. The time it takes a sound wave in the region ahead of the bow shock to travel upstream 1.2 times the length of the wave has elapsed.

obtained using the method of characteristics. The flow was simulated using a 50×50 grid for 200 steps, so that an upstream signal had time to move across the computational region.

In Figs. 6a and b we show the initial and final shock positions together with the isopycnic (constant density) contours. In Figs. 7a and b we show the initial and final density distributions along the two sides of the shock. Figures 8a, b and 9a, b
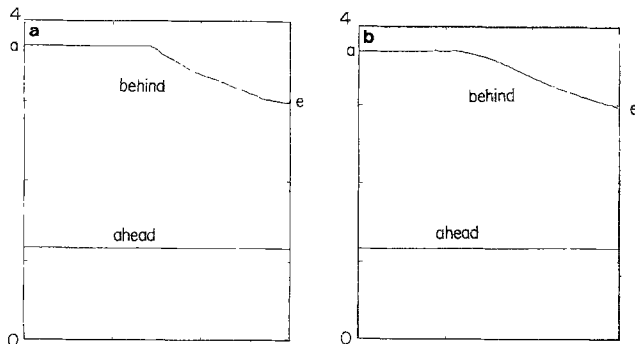

FIG. 7. (a, b) Initial and final density distributions along the two sides of the bow shock are plotted vs distance along the shock, from the attachment point (a) of the bow shock to its exit point (e), for the computation described in Fig. 6b.
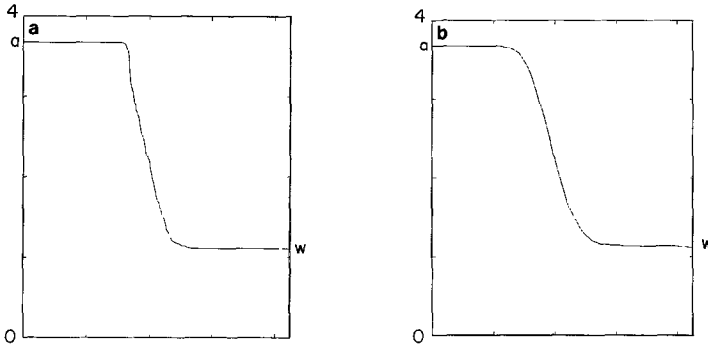
FIG. 8. (a, b) Initial and final density distributions along the wedge are plotted vs distance along the wedge, from the attachment point (a) of the bow shock to the exit point (w) of the wedge, for the computation described in Fig. 6b.

show the analogous density distributions along the wedge and along the portion of the exit below the shock, respectively. These figures indicate that the front tracking scheme accurately reproduces the steady-state solution. In this test it was especially important to apply the boundary conditions along the wedge correctly.

6.3. The Kelvin–Helmholtz Instability

The classical Kelvin–Helmholtz instability concerns two fluids separated by an interface across which there is a discontinuity in the tangential velocity. Such a flow configuration is unstable against a sinusoidal perturbation of the interface. In the regime where the amplitude is small relative to the wavelength, a first-order correction to the linearized equations provides a comparison solution. As illustrated in Fig. 10, we look for a periodic solution of the equations of gas dynamics that reduces, in the limit where the amplitude of the slip line is small, to a flow with constant density and pressure throughout, and constant particle velocity v_0 above and
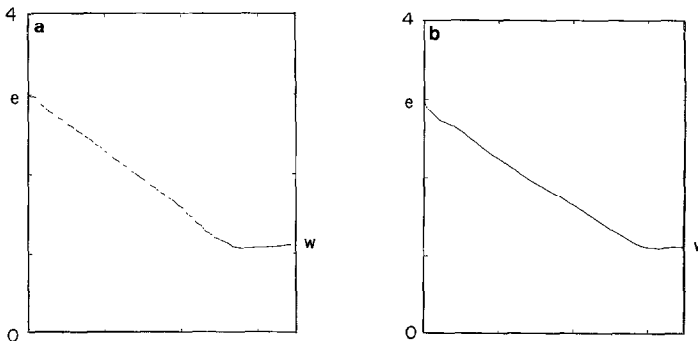

FIG. 9. (a, b) Initial and final density distributions along the exit are plotted vs distance along the exit, from the exit point (e) of the bow shock down to the wedge (w), for the computation described in Fig. 6b.
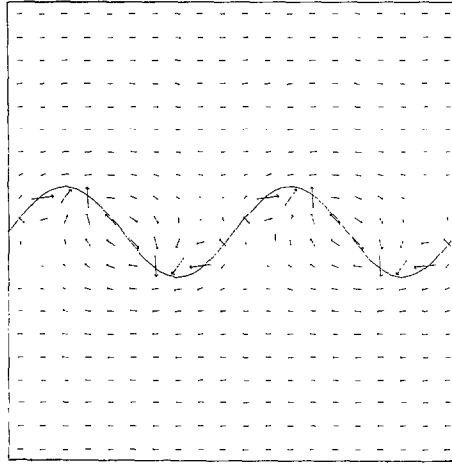
FIG. 10. The flow configuration for the Kelvin–Helmholtz instability is plotted. There is a sinusoidal slip line (solid line) separating the region above from the region below. In the regime where the amplitude of the slip line is small the density and pressure are almost constant throughout the flow, while the fluid velocities are approximately horizontal, with the velocity above equal and opposite to the velocity below.
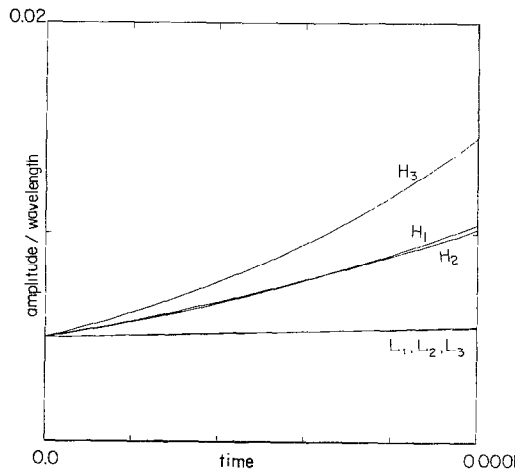

FIG. 11. A plot of the amplitude in the slip line vs time is shown for the Kelvin–Helmholtz instability in the small amplitude regime. For the curves (L_1-L_3) (which are indistinguishable in this graph) the jump in the velocity has Mach number 0.1, while for the curves (H_1-H_3) the jump in the velocity has Mach number 1. In each case curve 1 was obtained numerically using a 20×20 grid, whereas curves 2 and 3 were obtained for compressible and incompressible flow, respectively, using perturbation analysis in the amplitude of the slip line. At the higher Mach number it is important to model the significant compressibility effects.

$-v_0$ below. By linearizing the conservation of mass and Crocco's equations one obtains [19] the wave equation for the velocity potential. The solution exhibits an exponentially growing sinusoidal interface with a growth rate that depends on the jump $2 v_0/c_0$ in the Mach number of the free stream and on the distance to the boundaries. The corresponding result obtained assuming incompressibility of the fluid is obtained in the limit of vanishing Mach number.

The results of our numerical experiments are shown in Figs. 11 and 12a–c. Figure 11 is a plot of the amplitude of the sinusoidal slip line as a function of time for a small initial perturbation (amplitude-to-wavelength ratio of 0.005). There are two cases, corresponding to Mach numbers jump 1 and 0.1. The result from the linear analysis, both compressible and incompressible, are superimposed. As this plot demonstrates, the growth rate is accurately calculated even in the regime where methods for incompressible fluids are invalid.

Calculations were also performed in the large amplitude regime. The initial flow field, shown in Fig. 10, was obtained using the perturbation formulae at an amplitude-to-wavelength ratio of 0.2 and Mach number jump 0.4. Figures 12a and b show the slip line and the monumentum density vectors as computed with a 20×20 grid and a 40×40 grid, respectively. Figure 12c shows the slip line for the same run as computed with an 80×80 grid. The slip lines for all three runs are superposed in Fig. 12d. All three runs agree in the general form of the slip line. The finer grids show evidence of vortex formation and roll-up at shorter wavelengths. We stress, though, that even the qualitative shape of the slip line is extremely sensitive to the initial flow conditions. For instance if the initial slip line is taken to be purely sinusoidal in the vorticity rather than in the horizontal displacement [15], the slip line we calculate evolves into a single tight spiral. The authors know of no comparison solution for this problem, which involves the effects of the compressibility of the fluid and the presence of boundaries, but the results are in qualitative agreement with incompressible calculations.

6.4. Regular Reflection of a Shock Wave

Finally, the numerical solution for non-steady regular reflection of a shock wave reflections were compared with experimental results [4]. In the test problem a shock with Mach number is $M_S = 2.05$ is incident on a wedge with angle $\theta_W = 63.4°$.

We started the calculations with a small reflected shock enclosing a region (called the bubble) one-quarter of a mesh interval in height and with almost arbitrary data inside. The calculations were somewhat unstable in the neighborhood of the corner for a bubble smaller than two mesh intervals in height. After the bubble was higher than four mesh intervals the effects of the instability were not significant. At this stage of the run we found that the solution had settled down to its self-similar form and was largely independent of the initial data. In Fig. 13a the isopycnic (constant density) contours that we obtained numerically are shown at two stages in the run. In Fig. 13b the wall density distribution obtained in our calculations at the end of the run is superimposed on the experimental data.
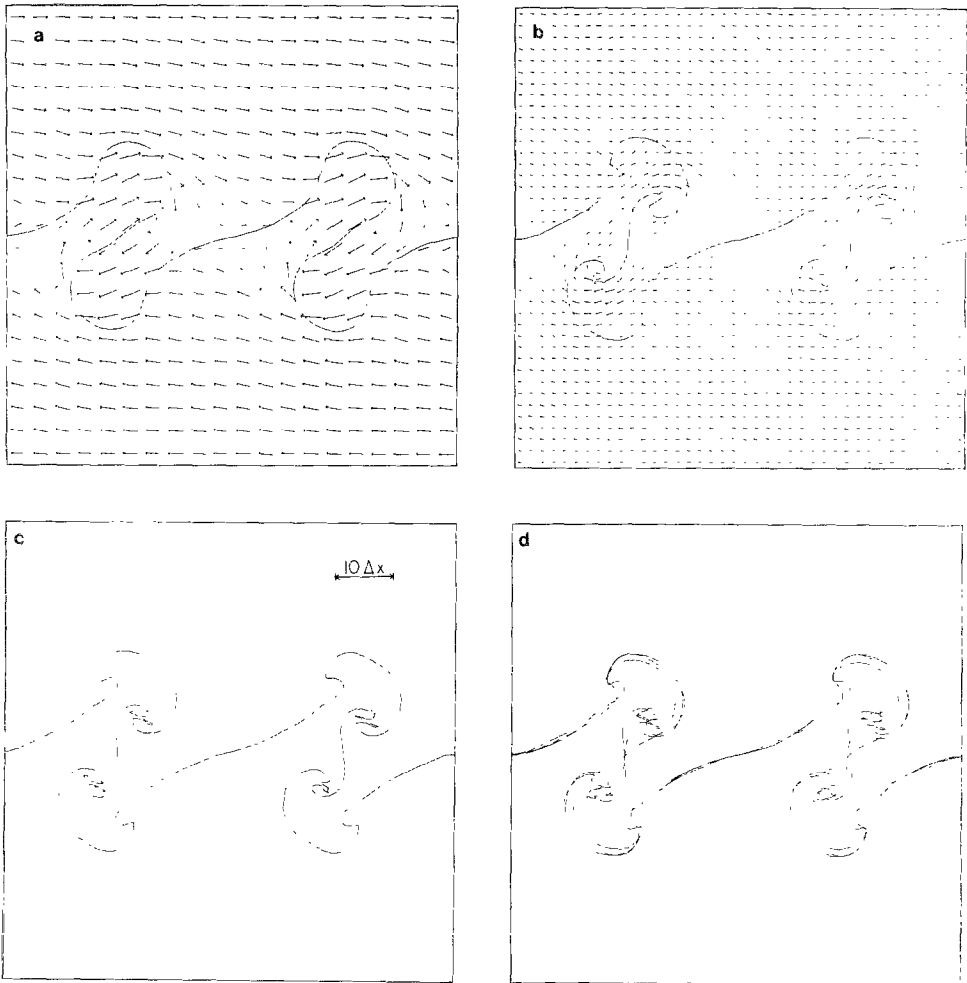
FIG. 12. (a) The slip line and the monumentum densities are shown for the Kelvin–Helmholtz instability with a large amplitude. The calculation was made on a 20×20 grid. The initial data, shown in Fig. 10, were obtained by the perturbation analysis for a velocity jump with Mach number 0.4. The time it takes a sound wave to travel 0.72 wavelength has elapsed. In the large amplitude regime the slip line no longer remains sinusoidal, but rather rolls up as vortices are formed. (b) The slip line and the monumentum densities are plotted for the problem described in (a), as calculated on a 40×40 grid. (c) The slip line is plotted for the problem described in Fig. (a), as calculated on an 80×80 grid. (d) The slip line positions, as computed on 20×20, 40×40, and 80×80 grids, are superposed for the problem described in (a). Fine structure in the vortices and in the shape of the slip line becomes evident under refinement of the computational grid. The authors know of no comparison solution for this problem.
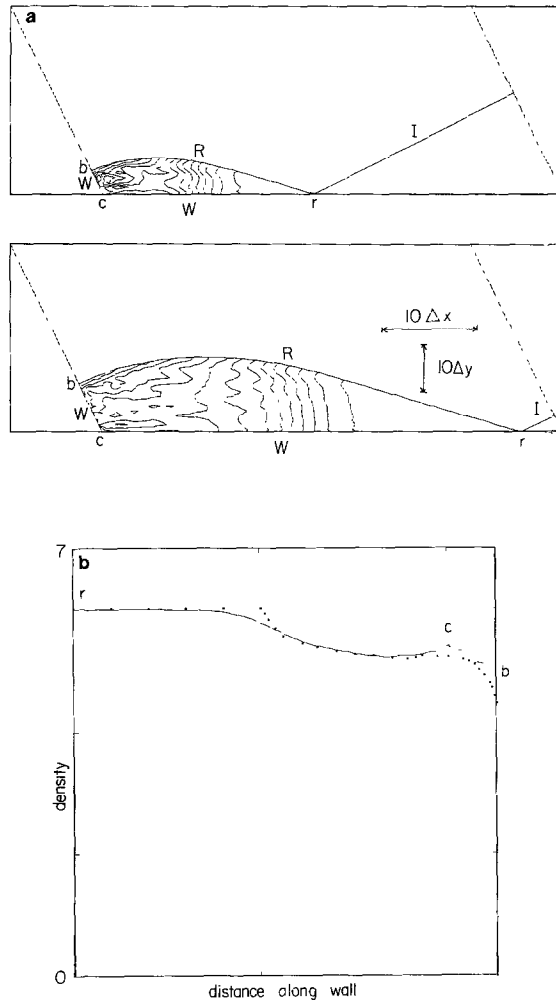
CHERN ET AL.

FIG. 13. (a) The isopycnic (constant density) contours are shown for a regular reflection problem in which an incident shock (I), moving downward and to the right into ambient gas, impinges on a reflecting wall (W) and reflects at point (r) to form a reflected shock (R). In this computation the Mach number of the incident shock is 2.05, and the angle of incidence of the shock on the wall is 26.6°. The calculations were performed on a 60×40 grid. (b) The density distribution along the wall for the problem described in (a) is plotted vs distance along the wall. The solid curve was obtained by numerical calculation, while the dots show the experimental results for air obtained by Deschambault and Glass [4].

7. Conclusions

We have seen that front tracking gives correct results for a series of test problems in compressible fluid dynamics. Computations on even coarse grids give satisfactory answers for the problems considered here. For example, in the regular reflection run, convergence to the self-similar solution has occurred when the region enclosed by the reflected shock is about 5 mesh blocks high. In the runs with circularly symmetric initial data, the contact and shock are initially separated by 0.4 mesh block, while by the middle of the run they are separated by 3 mesh blocks. Successful solution of test problems on coarse grids is critically important if complicated problems are to be solved on computers available within the near future. Also, the ability to handle bifurcations in the front topology is important for complicated problems. This capability exists at present for the oil reservoir version of front tracking [9] and is currently being implemented for gas dynamics.

Exactly the same source code for the interface, front, hyperbolic, driver, and utility libraries has been applied to diverse physical applications. The front tracking code is a large code, but its modular structure has minimized the problems typically associated with the development and use of such codes. The multiple applications have encouraged a more universal approach to the portions of the code for which generality is appropriate. Moreover, each application has benefited from progress necessitated by special difficulties in other applications. See [7-9, 13] for validation of front tracking for incompressible flow and for oil reservoirs. Thus front tracking has been fruitful in providing a general framework for the numerical solution of

References

1. M. Ben-Artzi and J. Falcovitz, *J. Comput. Phys.* **55** (1984), 1–32.
2. P. Colella and P. Woodward, *J. Comput. Phys.* **54** (1984)
3. R. Courant and K. Friedrichs, "Supersonic Flow and Shock Waves," Interscience, New York, 1948.
4. R. Deschambault and I. Glass, *J. Fluid Mech.* **131** (1983), 27–57.
5. H. Emmons, "Fundamentals of Gas Dynamics," Princeton Univ. Press, Princeton, N.J., 1958.
6. H. Glaz and T.-P. Liu, The asymptotic analysis of wave interactions and numerical calculations of transonic nozzle flow, preprint, 1982.
7. J. Glimm, E. Isaacson, B. Lindquist, O. McBryan, and S. Yaniv, in "Frontiers in Applied Mathematics," Vol. 1, pp. 137–160, SIAM, Philadelphia, 1983.
8. J. Glimm, B. Lindquist, O. McBryan, and L. Padmanabhan, in "Frontiers in Applied Mathematics," Vol. 1, pp. 107–135, SIAM, Philadelphia, 1983.
9. J. Glimm, B. Lindquist, O. McBryan, B. Plohr, and S. Yaniv, in "Proceedings, Seventh SPE Symposium on Petroleum Reservoir Simulation, 1983."
10. J. Glimm, D. Marchesin, and O. McBryan, *J. Comput. Phys.* **39** (1981), 179–200.
11. J. Glimm, G. Marshall, and B. Plohr, *Adv. Appl. Math.* **5**, No. 1 (1984), 1–30.
12. J. Glimm and O. McBryan, A computational model for interfaces, *Adv. Appl. Math.*, to appear.
13. J. Glimm, O. McBryan, R. Menikoff, and D. Sharp, Front tracking applied to Rayleigh–Taylor instability, *SIAM J. Sci. Stat. Computing*, to appear.

CHERN ET AL.

14. J. GUCKENHEIMER, *Arch. Rational Mech. Anal.* **59**, No. 3 (1975), 281–291.

15. R. KRASNY, "A Numerical Study of Kelvin–Helmholtz Instability by the Point Vortex Method," Thesis, Department of Mathematics, University of California, Berkeley, 1984.

16a. B. LINDQUIST, Construction of solutions for two dimensional Riemann problems, Adv. Hyperbolic Partial Diff. Eqs., Computers and Math. with Applications, to appear.

16b. B. LINDQUIST, The scalar Riemann problem in two spatial dimensions: piecewise smoothness of solutions and its breakdown. *SIAM J. Anal.*, to appear.

17. G. MARSHALL AND B. PLOHR, *J. Comput. Phys.* **56** (1985), 410.

18. G. MORETTI, "Thoughts and Afterthoughts about Shock Computations," Report No. PIBAL-72-37, Polytechnic Institute of Brooklyn, 1972.

19. B. PLOHR, J. GLIMM, AND O. MCBRYAN, *in* "Lecture Notes in Engineering, Vol. 3" (J. Chandra and J. Flaherty, Eds.), pp. 180–191, Springer-Verlag, New York, 1983.

20. R. RICHTMYER AND K. MORTON, "Difference Methods for Initial Value Problems," Interscience, New York, 1967.

21. J. SMOLLER, "Shock Waves and Reaction-Diffusion Equations," Springer-Verlag, New York, 1982.

22. G. SOD, *J. Fluid Mech.* **83** (1977), 785–794.

23. D. WAGNER, *SIAM J. Math. Anal.* **14**, No. 3 (1983), 534–559.

24. J. GLIMM, C. KLINGENBERG, O. MCBRYAN, B. PLOHR, D. SHARP, AND S. YANIV, Front tracking and two dimensional Riemann problems, *Adv. Appl. Math.*, to appear.